Supplementary Information for

Short-Range Order Enhances Strength and Tensile Ductility in Nanocrystalline Silver with Intercalation of Amorphous Nickel Nanolayers

Frederic Sansoz[*, a] *Malcolm R. Pringle,*[a] *Jin-Su Oh,*[b] *Lin Zhou*[b], *Ryan T. Ott*[b], *Yushun Liu,*[c] *Guo-Zhen Zhu*[c] and *Chuang Deng*[c]

[a] Department of Mechanical Engineering, The University of Vermont, Burlington, Vermont (USA)
[b] Division of Materials Science and Engineering, Ames National Laboratory, Ames, Iowa (USA)
[c] Department of Mechanical Engineering, University of Manitoba, Winnipeg, Manitoba (Canada)

*Corresponding Author: Frederic Sansoz, frederic.sansoz@uvm.edu

Content:

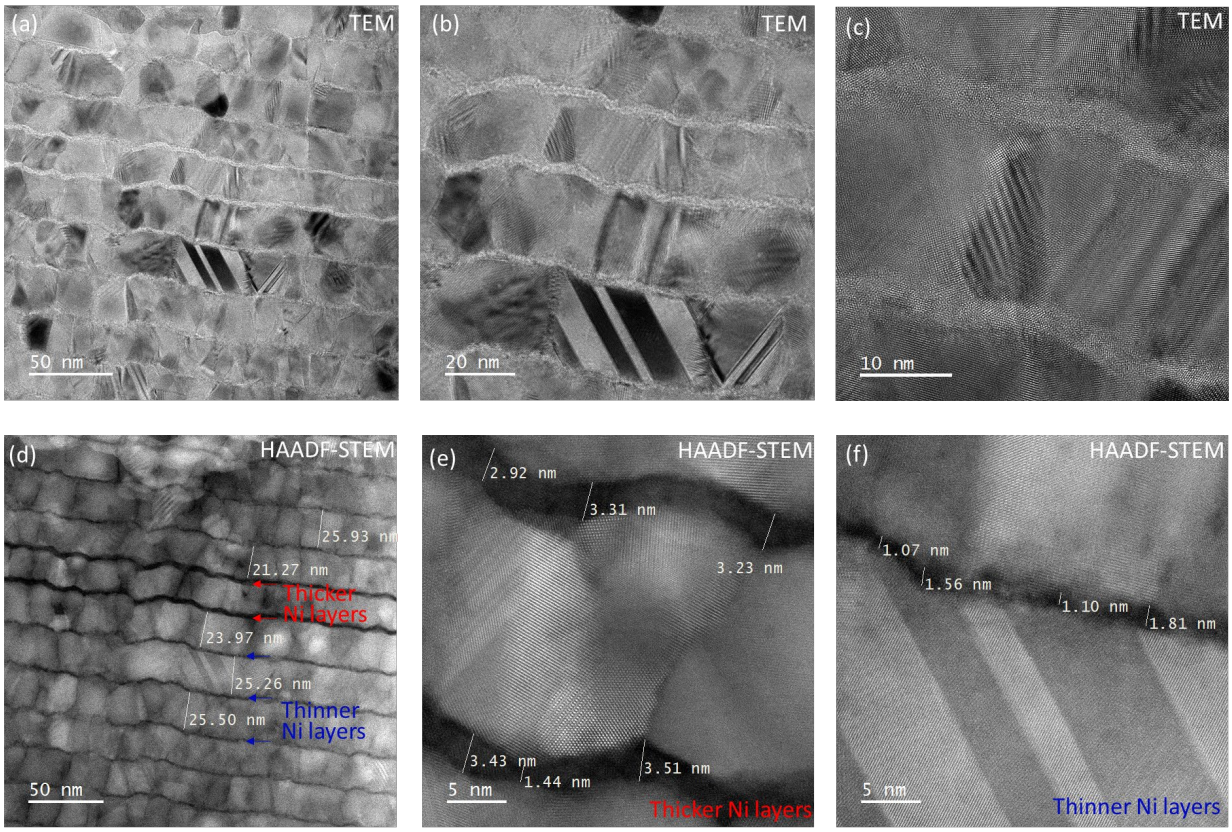

Figure S1: Thickness characterization of the Ni nanolayers by TEM and HAADF-STEM.

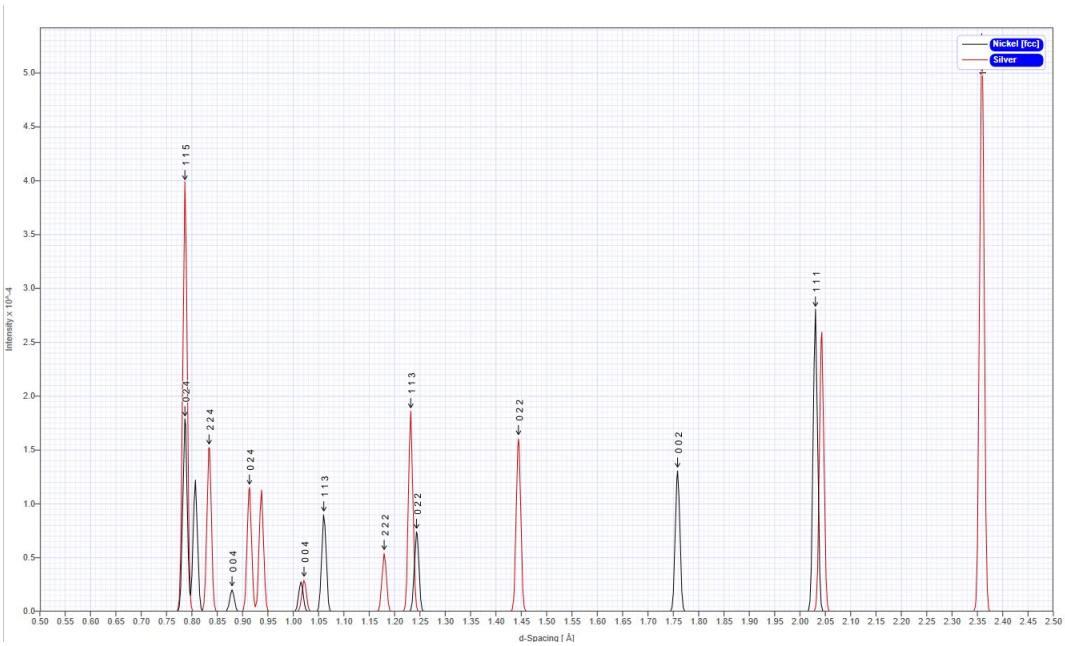

Figure S2: Reference electron diffraction intensities for face-centered cubic (fcc) Ni and Ag.

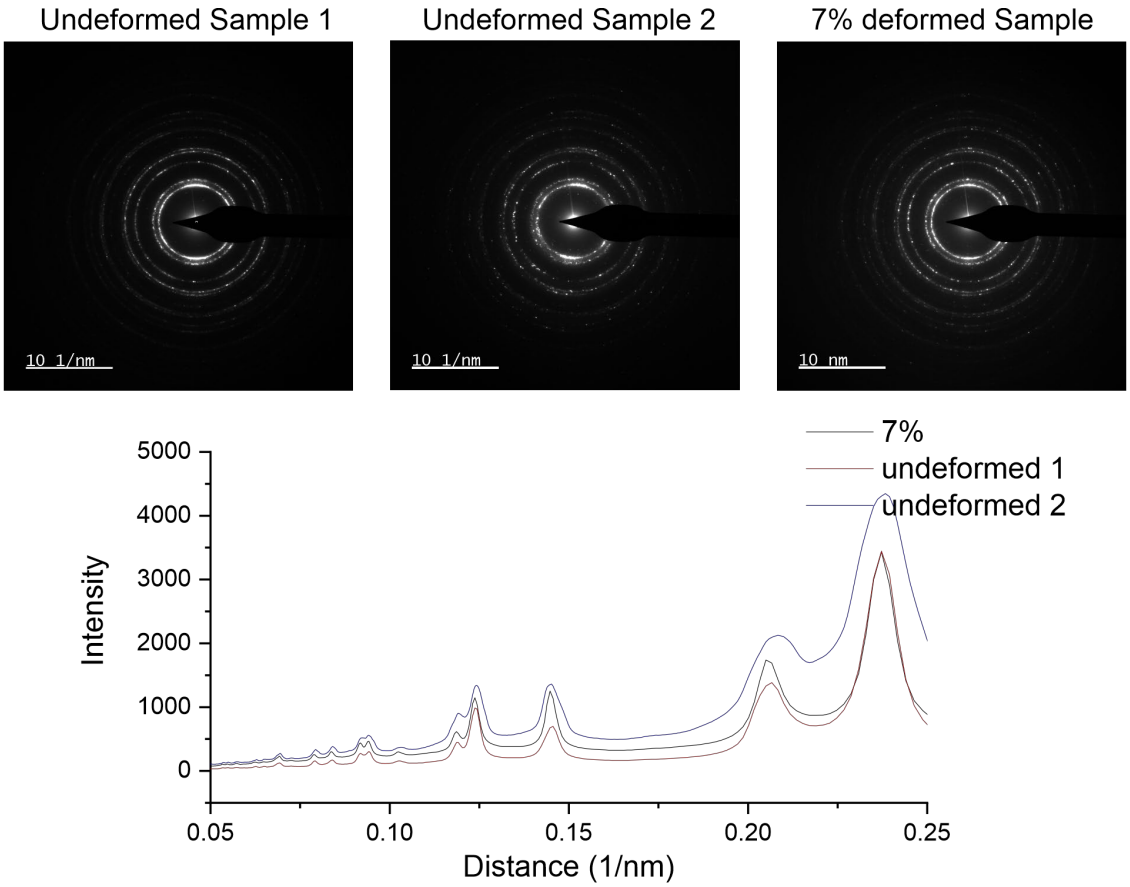

Figure S3: TEM electron diffractions in different samples before and after tensile deformation up to 7%.

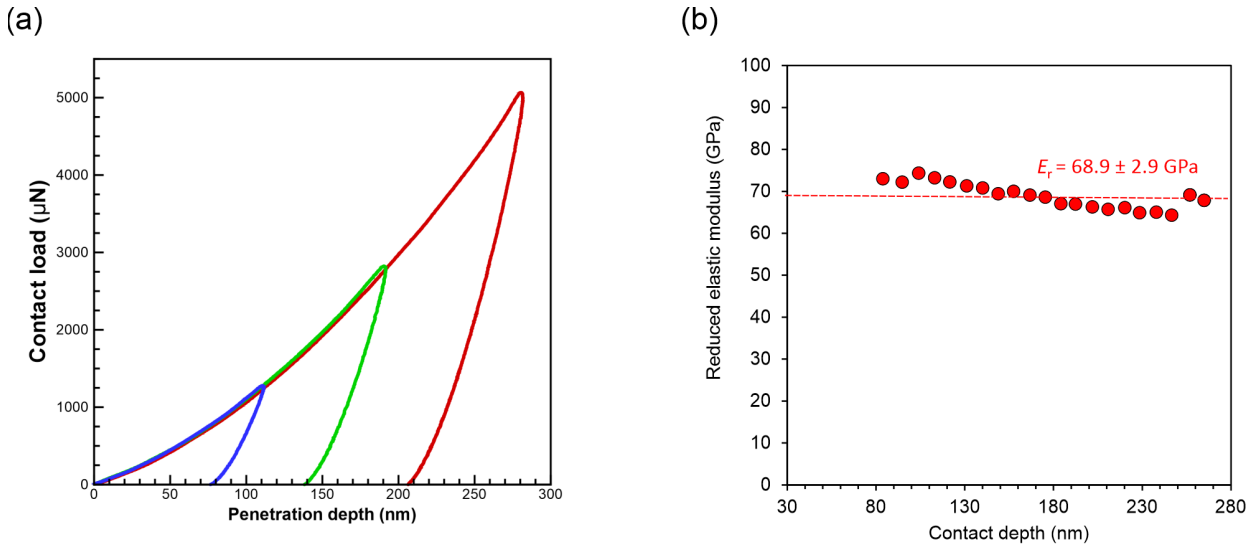

Figure S4: Nanoindentation measurements on sputtered nanocrystalline Ag intercalated with amorphous Ni nanolayers.

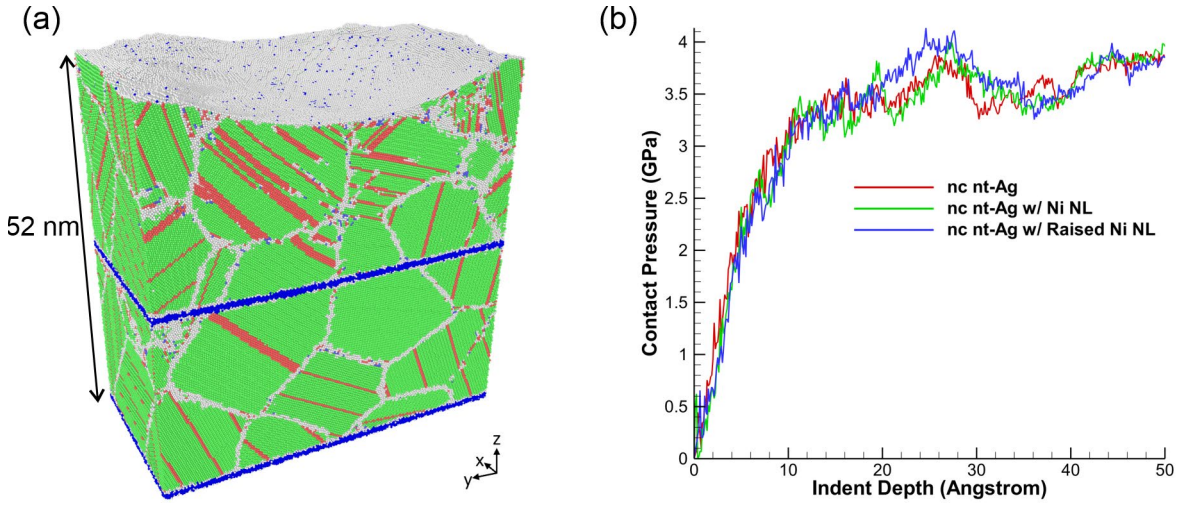

Figure S5: Atomistic simulation of nanoindentation of nanocrystalline Ag intercalated with amorphous pure Ni nanolayers. (a) Atomistic model used. (b) Computed contact pressure as a function of indentation depth for pure nanocrystalline-nanotwinned Ag (nc nt-Ag) and two Ni-intercalated nanocrystalline Ag models as shown in **Figures 2(c), 2(d) and 2(e)**.

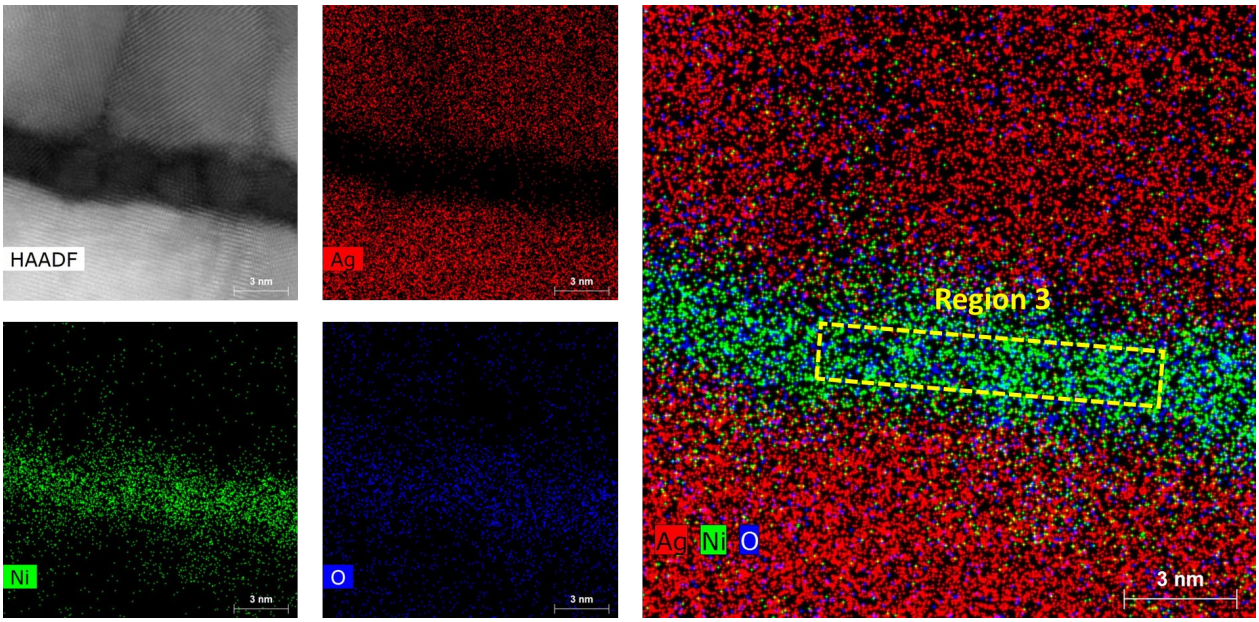

Figure S6. Chemical analysis by HAADF-STEM in a different Ni nanolayer region.

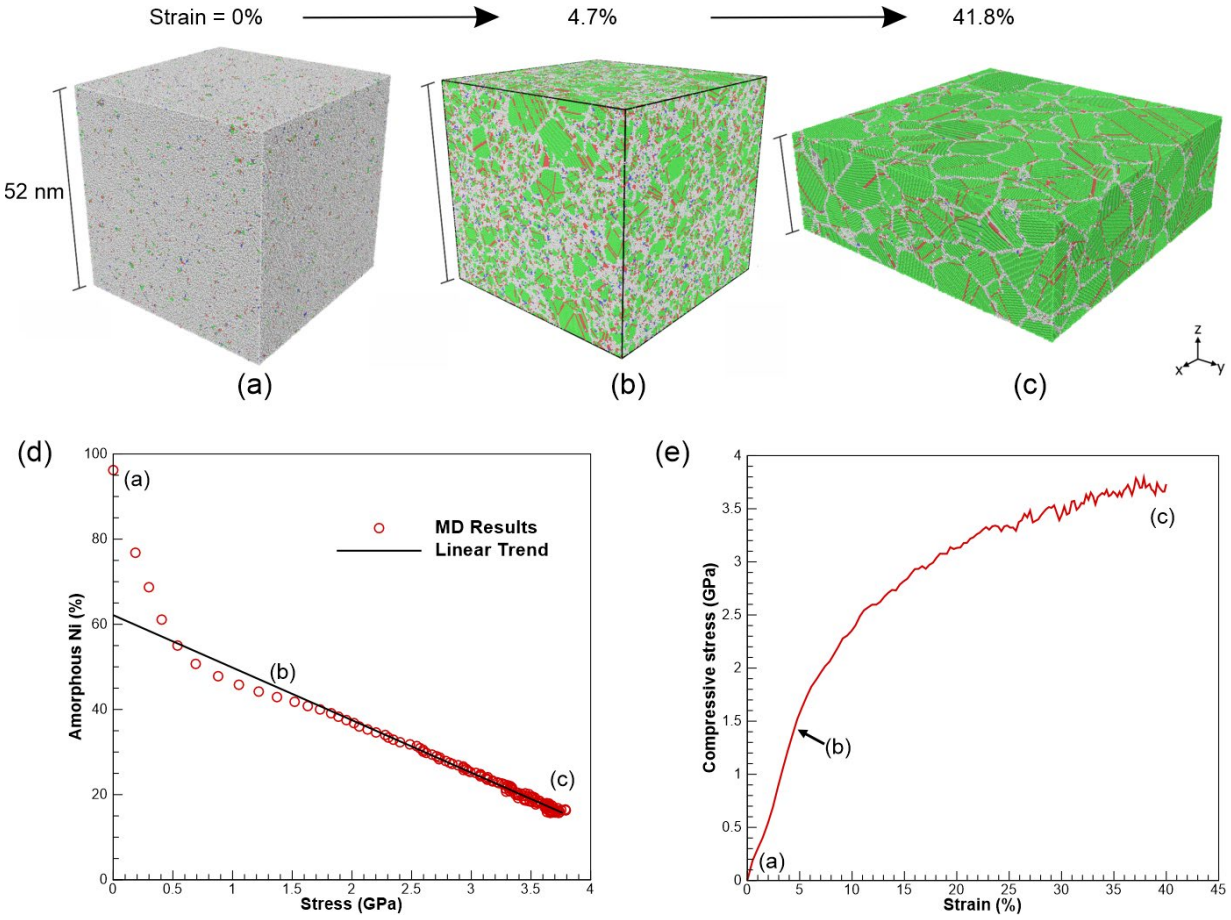

Figure S7: Molecular dynamics simulation of mechanical behaviour and recrystallization of a fully amorphous pure Ni phase under compression. (a) 96.2% amorphous Ni phase at 0% strain. (b) Semi-crystalline Ni with 41.8% amorphous phase at 4.7% strain. (c) Polycrystalline Ni with 15.7% amorphous grain boundaries at 42.5% strain. (d) Corresponding stress - strain curve and (e) amorphous Ni percent as a function of stress.

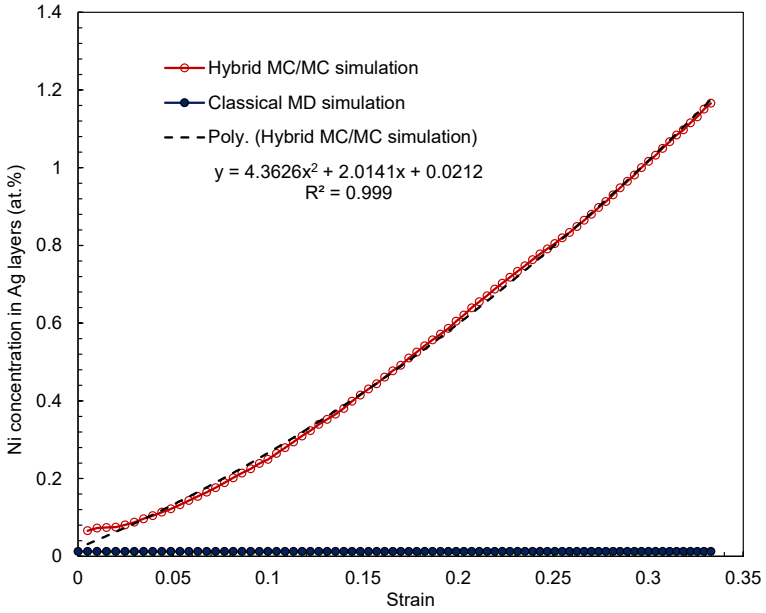

Figure S8: Change in Ni concentration within only Ag layers as a function of applied strain in the simulated Ni-intercalated nanocrystalline Ag nanolaminates (h = 3.0 nm).

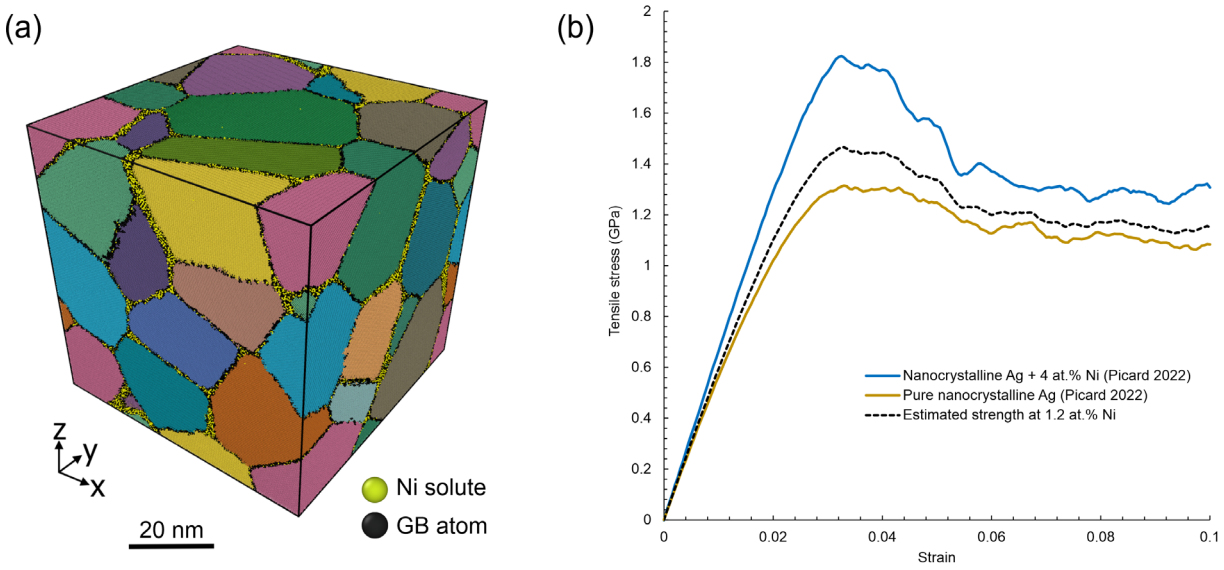

Figure S9: Upper strength estimate for a nanocrystalline Ag polycrystal (grain size = 24 nm) with 1.2 at.% Ni based on previous hybrid MC/MD simulation results on pure Ag and Ag-4 at.%Ni in E.A. Picard and F. Sansoz, Acta Materialia 240, 118367 (2022). (a) Atomistic model used by Picard. (b) Simulated tensile stress-strain curves by Picard and strength estimate proposed in the present study. The estimate corresponds to less than 5% strength increase between 7% and 11% applied strain.

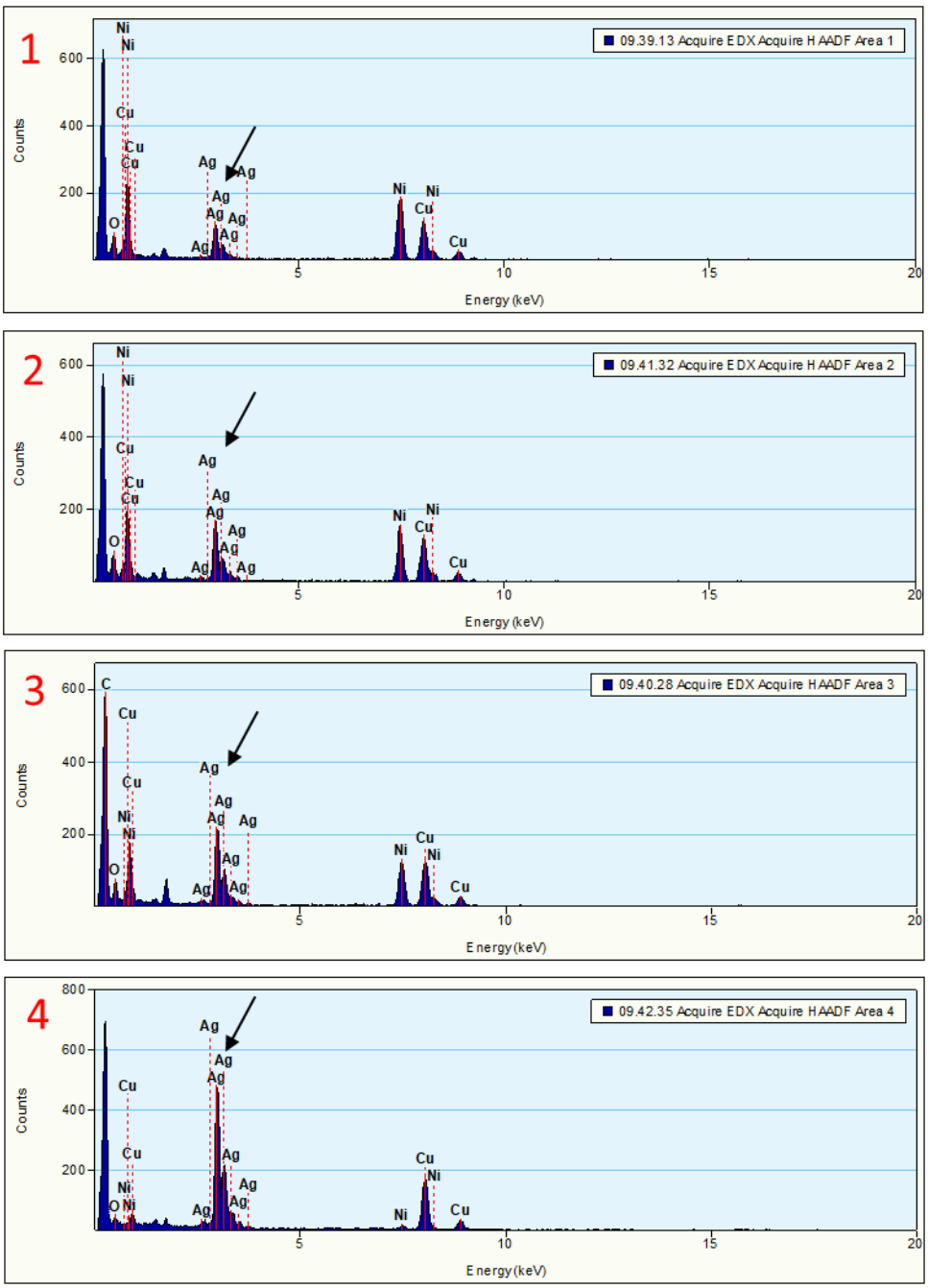

Figure S10: HAADF-EDX chemical analysis in the spots shown in **Figure 6(e)** that reveals different Ag concentrations within the amorphous Ni nanolayers in the plastically deformed material.

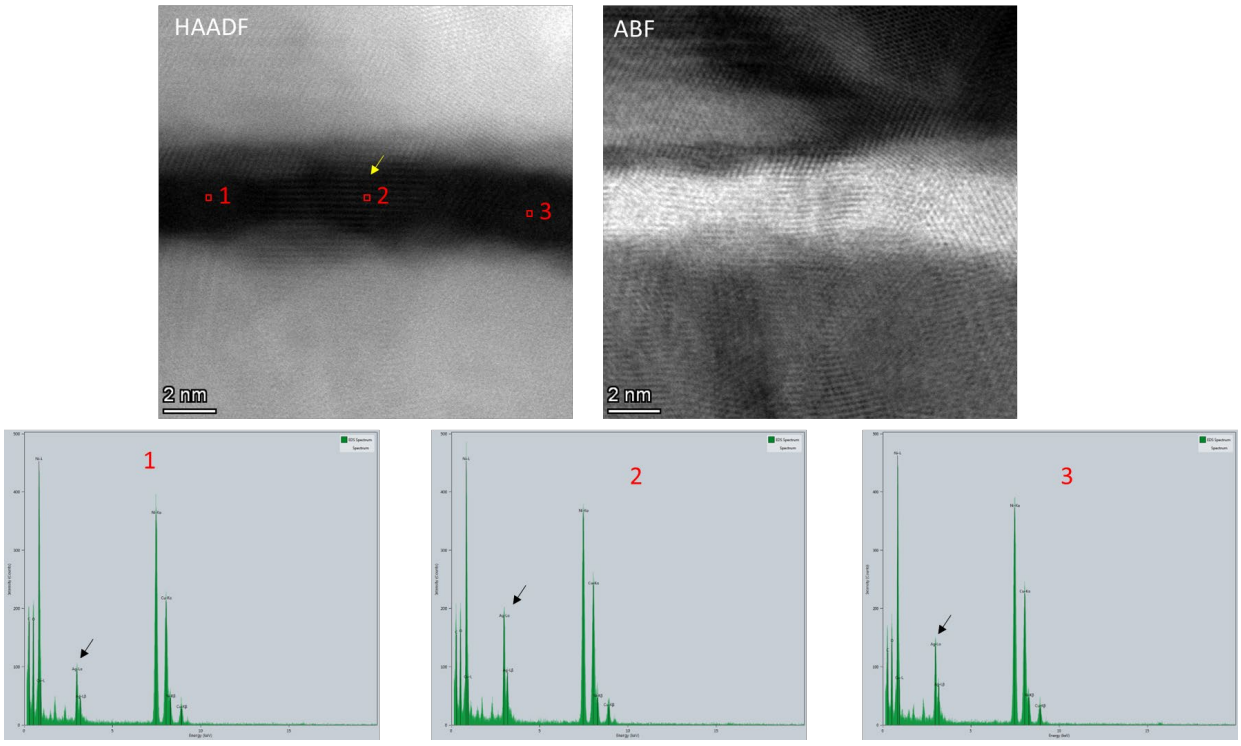

Figure S11: STEM-EDS (velox) analysis showing variation in Ag concentrations within the amorphous Ni nanolayers after 7% plastic deformation.

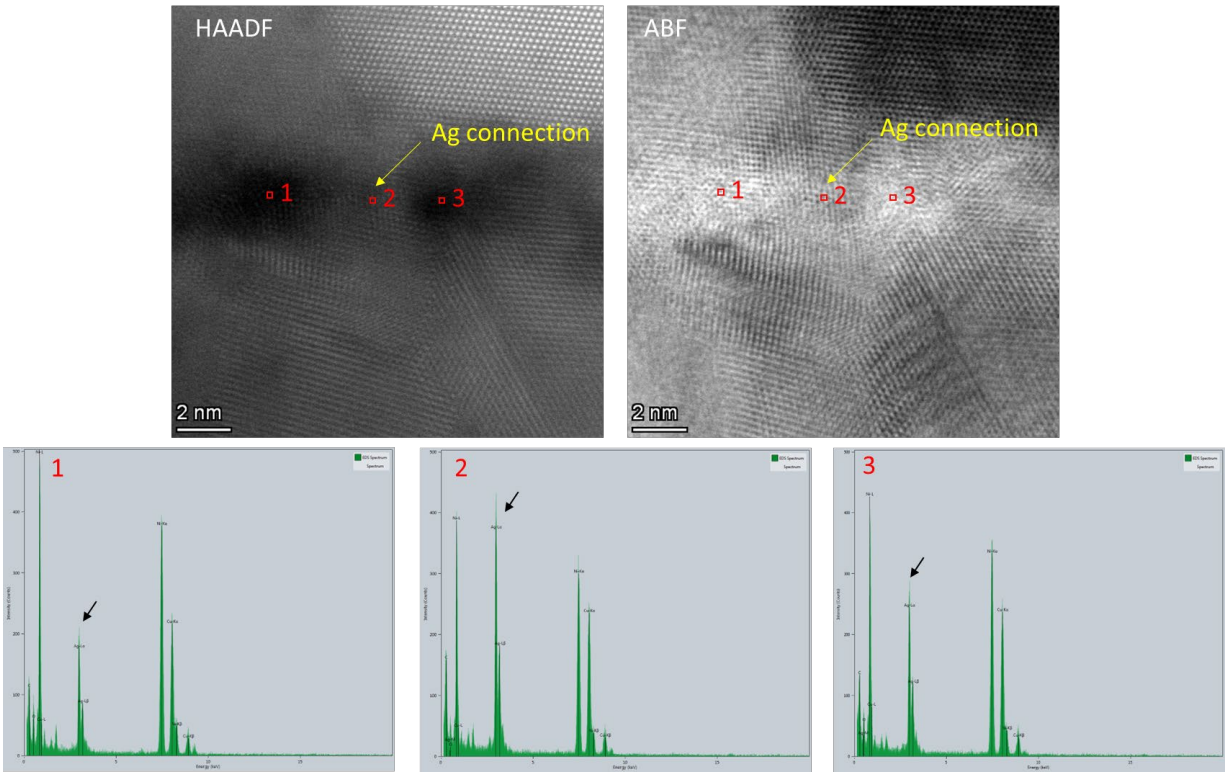

Figure S12: STEM-EDS (velox) analysis showing variation in Ag concentrations within the amorphous Ni nanolayers after 7% plastic deformation.

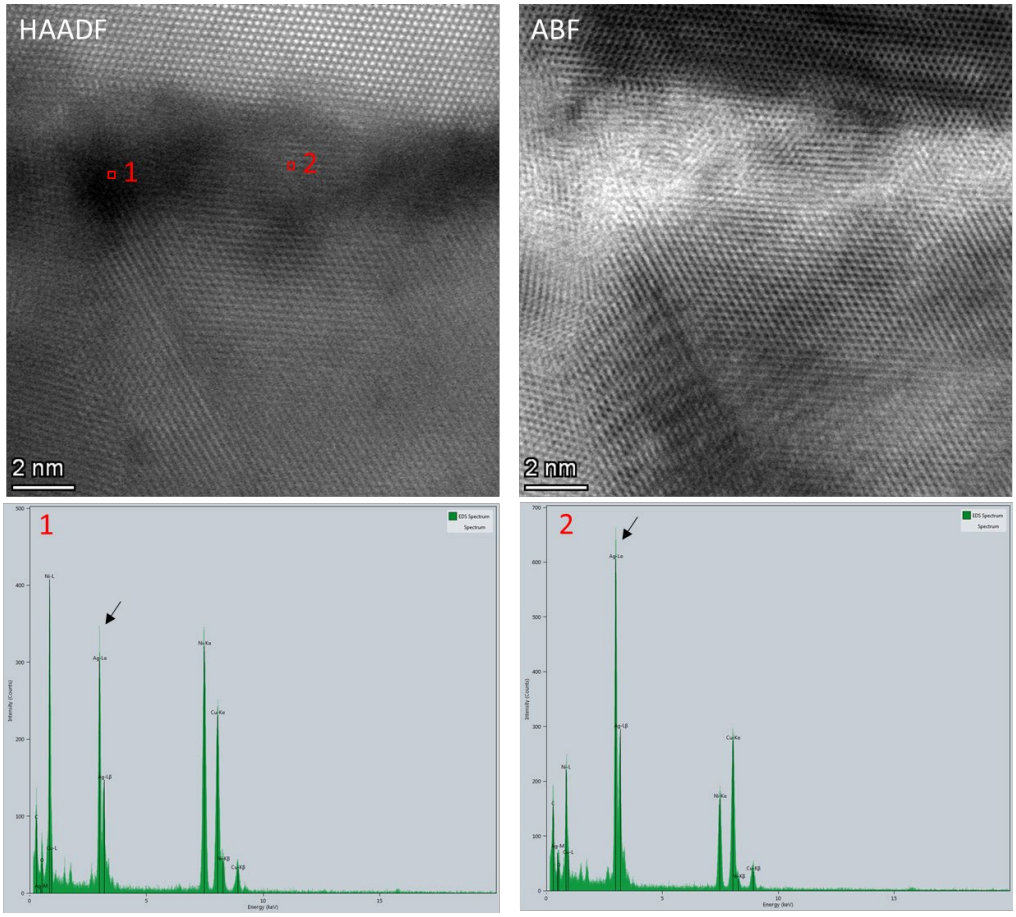

Figure S13: STEM-EDS (velox) analysis showing variation in Ag concentrations within the amorphous Ni nanolayers after 7% plastic deformation.

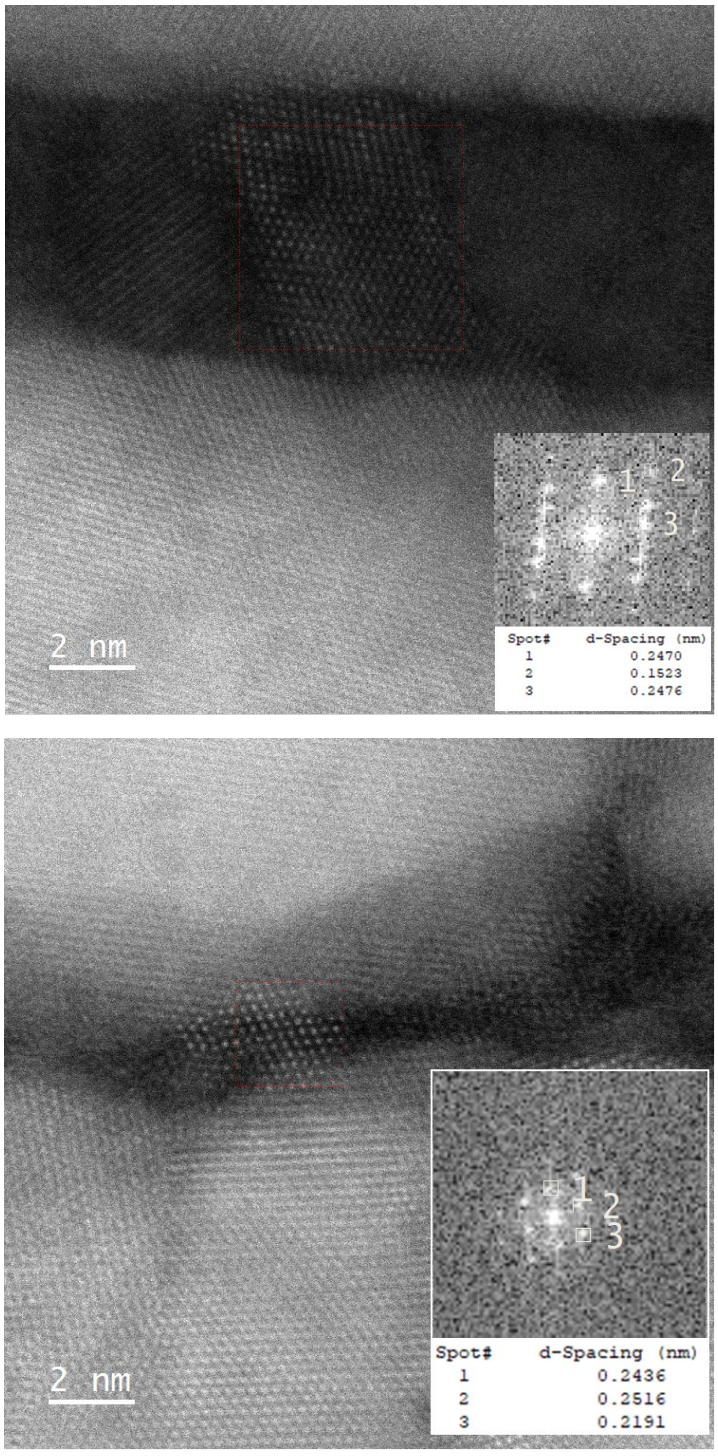

Figure S14: STEM image of short-range ordered connections formed inside an amorphous Ni nanolayer.

Table S1: Box composition of regions 1 and 2 in Figure 4(b2).

At%	Region 1	Region 2	Region 1 (only Ag and Ni)
Ag	4.27	97.53	8.1
Ni	48.44	2.21	91.9
O	47.20	0	-
S	0.10	0.25	-

Table S2: Box composition of region 3 in Supplementary Figure S6.

At%	Region 3	Region 3 (only Ag and Ni)
Ag	3.27	5.6
Ni	54.63	94.4
O	42.11	-